METAL-POOR, STRONGLY STAR-FORMING GALAXIES IN THE DEEP2 SURVEY: THE RELATIONSHIP BETWEEN STELLAR MASS, TEMPERATURE-BASED METALLICITY, AND STAR FORMATION RATE

Chun Ly[1,4], Jane R. Rigby[1], Michael Cooper[2], and Renbin Yan[3]
Submitted 2014 December 4

ABSTRACT

We report on the discovery of 28 $z \approx 0.8$ metal-poor galaxies in DEEP2. These galaxies were selected for their detection of the weak [O III]λ4363 emission line, which provides a "direct" measure of the gas-phase metallicity. A primary goal for identifying these rare galaxies is to examine whether the fundamental metallicity relation (FMR) between stellar mass, gas metallicity, and star formation rate (SFR) extends to low stellar mass and high SFR. The FMR suggests that higher SFR galaxies have lower metallicity (at fixed stellar mass). To test this trend, we combine spectroscopic measurements of metallicity and dust-corrected SFRs, with stellar mass estimates from modeling the optical photometry. We find that these galaxies are 1.05 ± 0.61 dex above the $z \sim 1$ stellar mass–SFR relation, and 0.23 ± 0.23 dex below the local mass–metallicity relation. Relative to the FMR, the latter offset is reduced to 0.01 dex, but significant dispersion remains (0.29 dex with 0.16 dex due to measurement uncertainties). This dispersion suggests that gas accretion, star formation and chemical enrichment have not reached equilibrium in these galaxies. This is evident by their short stellar mass doubling timescale of $\approx 100^{+310}_{-75}$ Myr that suggests stochastic star formation. Combining our sample with other $z \sim 1$ metal-poor galaxies, we find a weak positive SFR–metallicity dependence (at fixed stellar mass) that is significant at 97.3% confidence. We interpret this positive correlation as recent star formation that has enriched the gas, but has not had time to drive the metal-enriched gas out with feedback mechanisms.

Subject headings: galaxies: abundances — galaxies: distances and redshifts — galaxies: evolution — galaxies: ISM — galaxies: photometry — galaxies: starburst

1. INTRODUCTION

The chemical enrichment of galaxies, driven by star formation and modulated by gas flows from supernova and cosmic accretion, is key for understanding galaxy formation and evolution. The primary approach for measuring metal abundances is spectroscopy of nebular emission lines. These emission lines can be observed in the optical and near-infrared at $z \lesssim 3$ from the ground (e.g., Moustakas et al. 2011; Rigby et al. 2011; Henry et al. 2013a; de los Reyes et al. 2014) and space (e.g., Xia et al. 2012; Henry et al. 2013b; Whitaker et al. 2014b), and the *James Webb Space Telescope* will extend this to $z \sim 6$.

The most reliable metallicity measurements are made by measuring the flux ratio of the [O III]λ4363 line against [O III]λ5007. The technique is called the T_e or "direct" method because it determines the electron temperature (T_e) of the gas, and hence the gas-phase metallicity (Aller 1984). However, the detection of [O III]λ4363 is difficult, as it is weak, almost undetectable in metal-rich galaxies. Only 0.3% of the Sloan Digital Sky Survey (SDSS) has detected [O III]λ4363 at signal-to-noise (S/N) ≥ 2 (Izotov et al. 2006).

Efforts have been made to increase the number of galaxies with direct metallicities in the local universe (e.g., Brown et al. 2008; Berg et al. 2012; Izotov et al. 2012), and at $z \gtrsim 0.2$ (Hoyos et al. 2005; Hu et al. 2009;

Ly et al. 2014, hereafter Ly14); however, the total sample size is ∼120 (mostly in the local universe).

While the T_e method cannot be used for the full dynamic range of metallicity, detecting [O III]λ4363 is an effective way to identify metal-poor galaxies. Their low metallicity suggests that they are either (1) in their earliest stages of formation, (2) accreting metal-poor gas, or (3) undergoing significant metal-enriched gas outflows. The latter has received significant interest as Ellison et al. (2008) found that at a given stellar mass, lower-metallicity galaxies in the local universe tend to have higher SFRs. Thus, while the stellar mass–metallicity relation is tight (∼0.1 dex; Tremonti et al. 2004), it may be a projection of a non-evolving three-dimensional relationship between stellar mass ($M_\star$), gas-phase metallicity (Z), and SFR (e.g., Lara-López et al. 2010; Mannucci et al. 2010; Hunt et al. 2012).

However, the existence of a $M_\star$–Z–SFR relation remains controversial, as recent studies have yielded results that agree or disagree with predictions (see de los Reyes et al. 2014 and Salim et al. 2014 for a review). Moreover, the $M_\star$–Z–SFR relation has yet to be tested with large samples of metal-poor ($Z \lesssim 0.25\ Z_\odot$) galaxies, especially at higher redshift. The largest high-z metal-poor sample is that of Ly14 from the Subaru Deep Field (SDF), which detected [O III]λ4363 in 20 galaxies at $z \sim 0.4$–1. In this study, they found evidence that galaxies with the highest specific SFR (SFR/$M_\star$, hereafter sSFR) were not necessary more metal-poor. This result, based on 20 galaxies, requires further confirmation.

In this Letter, we identify 28 metal-poor galaxies from the DEEP2 Galaxy Redshift Survey (Davis et al. 2003; Newman et al. 2013). Unlike the majority of previous

---

[1] Observational Cosmology Laboratory, NASA Goddard Space Flight Center, 8800 Greenbelt Road, Greenbelt, MD 20771, USA;
[2] Center for Galaxy Evolution, Department of Physics and Astronomy, UCI, Irvine, CA, USA
[3] Department of Physics and Astronomy, University of Kentucky, Lexington, KY, USA
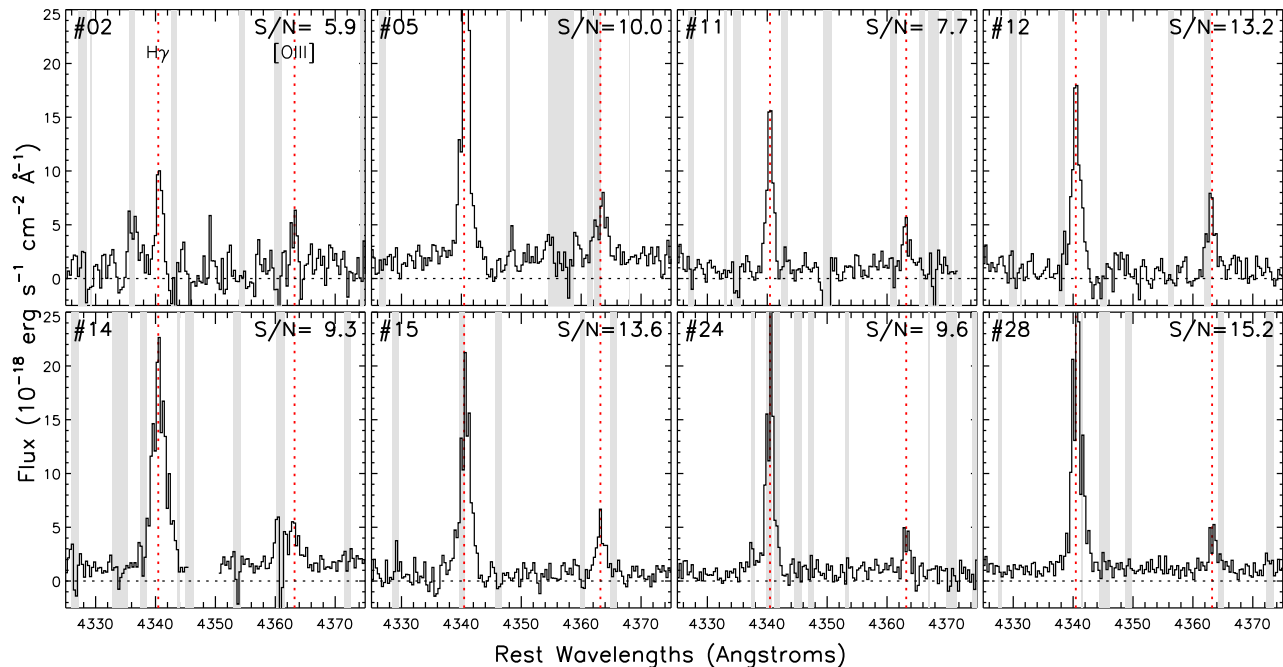[4] NASA Postdoctoral Fellow.

FIG. 1.— Detections of [O III]λ4363 in $z \sim 0.8$ DEEP2 galaxies. The Keck/DEIMOS spectra for 8 of 28 galaxies are shown by the solid black lines, with vertical red dashed lines indicating the locations of Hγλ4340 and [O III]λ4363. OH skylines are indicated by the grey shaded regions. The signal-to-noise of [O III]λ4363 detections is reported in the top right.

$M_\star$–Z–(SFR) relation studies that use strong-line metallicity calibrations, we follow Ly14 and Andrews & Martini (2013) (hereafter AM13) and obtain temperature-based metallicities. This is advantageous, as strong-line metallicities are problematic for high-z galaxies due to suspected differences in the physical conditions of the interstellar gas (e.g., Liu et al. 2008), but see also Juneau et al. (2014) for a different interpretation. These differences, if present, may be incorrectly interpreted as evolution in the metal content. Our sample of 28 galaxies substantially increases the number of $z \geq 0.25$ galaxies with S/N≥3 [O III]λ4363 detections by 65% (43 to 71).

Throughout this Letter, we adopt a cosmology with $\Omega_\Lambda = 0.7$, $\Omega_M = 0.3$, and $h = 0.7$, a Chabrier (2003) initial mass function (IMF), and a solar metallicity of $12 + \log(\mathrm{O/H}) = 8.69$.

2. THE SAMPLE

The DEEP2 Survey has surveyed $\sim$3 deg^2 over four fields using the DEIMOS multi-object spectrograph (Faber et al. 2003) on the Keck-II telescope. The survey has provided optical ($\approx$6500–9000Å) spectra for $\sim$53,000 galaxies brighter than $R_{\mathrm{AB}} = 24.1$, and precise redshifts for $\sim$70% of targeted galaxies. An overview of the survey can be found in Newman et al. (2013).

Using the fourth data release (DR4),[5] we select 37,396 sources with reliable redshifts (quality flag $\geq$3). We consider those with spectral coverage that spans 3720–5010 Å (rest-frame). This enable us to determine metallicity from oxygen and hydrogen emission lines ([O II]λλ3726,3729, [O III]λλλ4363,4959,5007, and Hβ), and further limits the sample to 4,140 galaxies at $z = $ 0.697–0.859 (average: 0.779).

We follow the approach of Ly14 that fits emission lines with Gaussian profiles using the IDL routine MPFIT (Markwardt 2009). Spectroscopic redshifts are used as

priors for the location of emission lines. With measurements of emission-line fluxes and the noise in the spectra (measured from a 200 Å region around each line), we select those with [O III]λ4363 and [O III]λ5007 detected at S/N≥3 and S/N≥100, respectively. This yields an initial sample of 54 galaxies. We inspect each spectrum and remove 26 galaxies from our sample, primarily because of contamination from OH sky-lines. This leaves 28 galaxies. One source (#21) was observed twice. The other spectrum also detected [O III]λ4363 at lower S/N, so the better spectrum is used in our analysis. Compared to the previous DEEP2 sample (Hoyos et al. 2005), we confirmed two, thus 26 galaxies in our sample are newly identified. Detections of [O III]λ4363 are shown in Figure 1, and galaxy properties are provided in Table 1. We illustrate in Figure 2 the emission-line luminosities, rest-frame equivalent widths (EWs), and $O_{32} \equiv$ [O III]/[O II] and $R_{23} \equiv$ ([O II]+[O III])/Hβ flux ratios (Pagel et al. 1979; McGaugh 1991), and compare our sample to local galaxies and other [O III]λ4363-detected galaxies (Ly14).

2.1. Flux Calibration

The publicly released data of DEEP2 are not flux-calibrated, which is problematic for measuring the 4363-to-5007 ratio, and hence T_e. To address this limitation, we use proprietary IDL codes developed by Jeffrey Newman, Adam Walker, and Renbin Yan of the DEEP2 team. These codes take into account the overall throughput, quantum efficiency of the eight CCD detectors, apply coarse telluric corrections for atmospheric absorption bands, and use the R and I DEEP2 photometry to transform the spectrum to energy units. The DEEP2 team has demonstrated that the calibration is reliable at the 10% level when compared to SDSS stars observed by DEEP2.
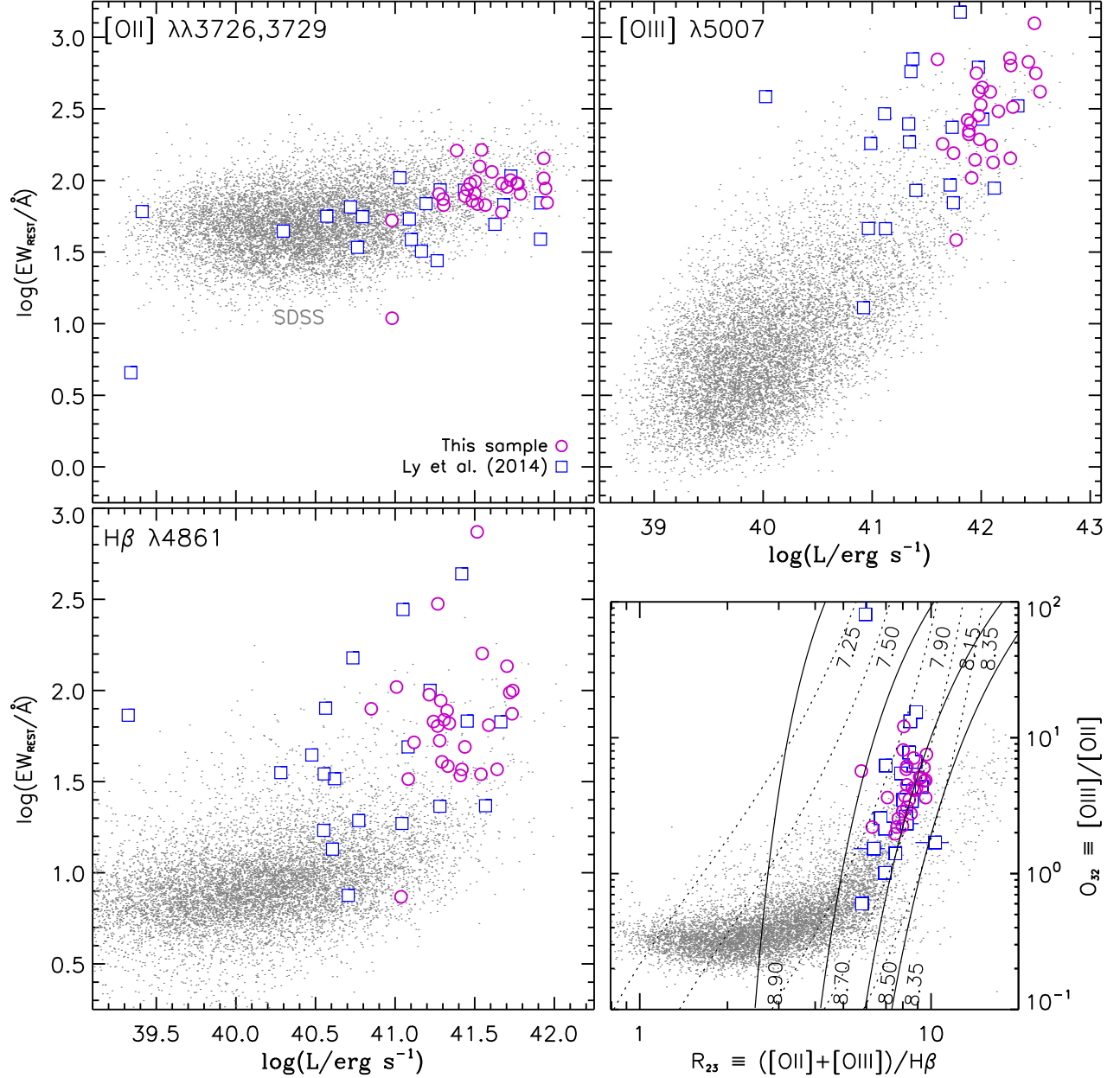
3. DERIVED MEASUREMENTS

FIG. 2.— Emission-line luminosities, flux ratios, and rest-frame EWs for our [O III]λ4363 sample (purple circles). All luminosities and flux ratios are observed, before correction for dust attenuation. Gray points illustrate the SDSS DR7 emission-line sample. The lower right panel shows the metallicity-sensitive (R_{23}) and ionization parameter-sensitive (O_{32}) emission-line ratios. Photoionization models from McGaugh (1991) are overlaid for metallicities between $12 + \log(\mathrm{O/H}) = 7.25$ and $12 + \log(\mathrm{O/H}) = 8.9$. Solid (dotted) curves are for metallicities on the "upper" ("lower") R_{23} branch. Overlaid as blue squares is the [O III]λ4363 detected sample from Ly14.

3.1. Dust Attenuation Correction from Balmer Decrements

To correct the emission-line fluxes for dust attenuation, we use Balmer decrement measurements. At $z \sim 0.8$, the existing DEEP2 optical spectra measure Hβ, Hγ, and Hδ. While these lines are intrinsically weak compared to Hα,[6] our galaxies possess high emission-line EWs, which result in 22, 26, and 28 galaxies having Hδ, Hγ, and Hβ detected at S/N$\geq$10, respectively. The significant detections enable dust attenuation measurements of $\sigma(\mathrm{A(H\alpha)}) \approx 0.1$ mag (average from Hγ/Hβ).

A problem encountered with Balmer emission lines is the underlying stellar absorption. Our examination of

each spectrum reveal weak stellar absorption, making it difficult to obtain reliable fits to the broad wings of absorption lines. To address this limitation, we stack our spectra. Here, the continuum (around each Balmer line) is normalized to one, and an average is computed with the exclusion of spectral regions affected by OH sky-line emission. Stellar absorption is detected in Hδ, and is consistent with an EW$_{\mathrm{rest}}$ correction of 1 Å. For our entire sample, we adopt an EW$_{\mathrm{rest}}$ correction of 1 Å for Hβ, Hγ, and Hδ. With these corrections for stellar absorption, we illustrate the Balmer decrements in Figure 3.

Assuming that the hydrogen emission originates from an optically thick H II region obeying Case B recombination, the intrinsic Balmer flux ratios are $(\mathrm{H\gamma/H\beta})_0 = 0.468$ and $(\mathrm{H\delta/H\beta})_0 = 0.259$. Dust absorption alters

---

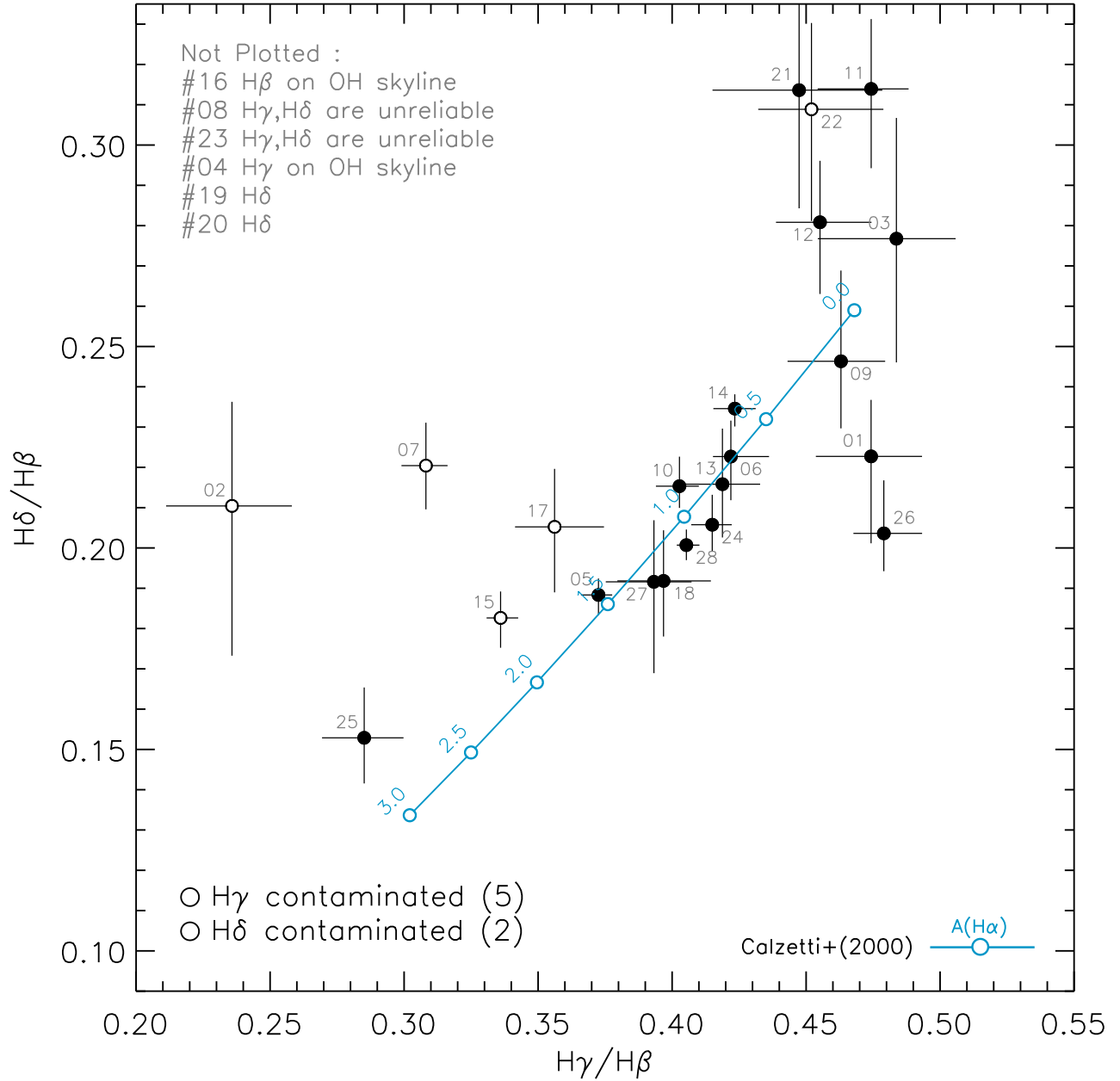[6] Hα is redshifted beyond the optical spectral coverage.

FIG. 3.— Balmer decrements (Hγ/Hβ and Hδ/Hβ) for our [O III]λ4363 sample. Reliable measurements are shown by the filled circles, while those affected by contamination from OH sky-line emission are shown as open circles. Blue circles and curve show the effects on the Balmer decrements with increasing dust reddening following Cal00. Values adjacent to blue circles indicate $A(\mathrm{H}\alpha)$. The significant scatter in the upper right is due to less reliable Hδ/Hβ measurements. These galaxies all have Hγ/Hβ measurements that are consistent with $A(\mathrm{H}\alpha) \sim 0$.

these observed ratios as follows:

$$\frac{(\mathrm{H}n/\mathrm{H}\beta)_{\mathrm{obs}}}{(\mathrm{H}n/\mathrm{H}\beta)_0} = 10^{-0.4E(B-V)[k(\mathrm{H}n)-k(\mathrm{H}\beta)]}, \qquad (1)$$

where $E(B–V)$ is the nebular color excess, and $k(\lambda) \equiv A(\lambda)/E(B–V)$ is the dust reddening curve. We illustrate in Figure 3 the observed Balmer decrements under the Calzetti et al. (2000) (hereafter Cal00) dust reddening formalism. We find that our Balmer decrements are consistent with Cal00. For the remainder of our Letter, all dust-corrected measurements adopt Cal00 reddening.

Our color excesses, are determined mostly (20/28) from Hγ/Hβ. For five galaxies, we use Hδ/Hβ since Hγ suffers from contamination from OH skylines. For the remaining 3 galaxies, the dust reddening could not be determined from either Balmer decrement (they were both

affected by OH sky-line emission). For these galaxies, we assume $E(B–V) = 0.22\pm0.23$ mag ($A(\mathrm{H}\alpha) \approx 0.73\pm0.75$ mag), which is the average of our sample. For Balmer decrements that imply negative reddening (6 cases), we adopt $E(B − V) = 0$ with measurement uncertainties based on Balmer decrement uncertainties.

3.2. T_e-based Metallicity Determinations

To determine the gas-phase metallicity for our galaxies, we follow previous direct metallicity studies and use the empirical relations of Izotov et al. (2006). Here, we briefly summarize the approach, and refer readers to Ly14 for more details. First, the O^{++} electron temperature, $T_e([\mathrm{O\,III}])$, can be estimated using the nebular-to-auroral [O III] ratio, [O III] $\lambda\lambda4959,5007/$[O III] $\lambda4363$. We

correct the above flux ratio for dust attenuation (Section 3.1). We also apply a 5% correction, since T_e determinations from Izotov et al. (2006) are found to be overestimated due to a non-equilibrium electron energy distribution (Nicholls et al. 2013).

Our [O III] measurements have a very large dynamic range. The strongest (weakest) [O III]$\lambda4363$ line is 6.5% (0.7%) of the [O III] $\lambda5007$ flux. We find that the average (median) $\lambda4363/\lambda5007$ flux ratio for our sample is 0.018 (0.015). The derived T_e for our galaxy sample spans (1–3.1)$\times10^4$ K.

To determine the ionic abundances of oxygen, we use two emission-line flux ratios, [O II] $\lambda\lambda3726,3729$/Hβ and [O III] $\lambda\lambda4959,5007$/Hβ. For our metallicity estimation, we adopt a standard two-zone temperature model with T_e([O II]) = $0.7T_e$([O III]) + 3000 (AM13), to enable direct comparisons to local studies. In computing O$^+$/H$^+$, we also correct the [O II]/Hβ ratio for dust attenuation. We do not correct [O III]/Hβ since the effects are negligible.

Since the most abundant ions of oxygen in H II regions are O$^+$ and O^{++}, the oxygen abundances are given by O/H = (O$^+$ + O^{++})/H$^+$. In Table 1, we provide estimates of T_e([O III]), and de-reddened metallicity for our sample. Our most metal-poor systems are #04 and #08, and can be classified as extremely metal-poor galaxies (≤0.1 $Z_\odot$).

3.3. *Dust-Corrected Star Formation Rates*

In addition to gas-phase metallicity, our data allow us to determine dust-corrected SFRs using the hydrogen recombination lines, which are sensitive to the shortest timescale of star formation, $\lesssim10$ Myr.

Assuming a Chabrier (2003) IMF with masses of 0.1–100 $M_\odot$, and solar metallicity, the SFR can be determined from the observed Hβ luminosity (Kennicutt 1998):

$$\frac{\text{SFR}}{M_\odot \text{ yr}^{-1}} = 4.4\times10^{-42} \times 2.86\times10^{0.4A(\text{H}\beta)}\frac{L(\text{H}\beta)}{\text{erg s}^{-1}}, \quad (2)$$

where $A(\text{H}\beta) = 4.6E(B–V)$. This relation overestimates the SFR at low metallicities due to the dependence of a stronger ionizing radiation field on lower metallicity. Since our galaxies have $Z \approx 0.2Z_\odot$, we reduce the SFRs by 37% (Henry et al. 2013b). Our SFR estimates are summarized in Table 1 and are illustrated in Figure 4. We find that our galaxies have dust-corrected SFRs of 0.8–130 $M_\odot$ yr^{-1} with an average (median) of 10.7 (4.6) $M_\odot$ yr^{-1}.

3.4. *Stellar Masses from SED Modeling*

To determine stellar masses, we follow the common approach of modeling the spectral energy distribution (SED) with stellar synthesis models (e.g., Salim et al. 2007; Ly et al. 2011, 2012). The eight-band photometric data include BRI imaging from the Canada-France-Hawaii Telescope (CFHT) for the DEEP2 survey (Coil et al. 2004). In addition, publicly available $ugriz$ imaging from the CFHT Legacy Survey is available in Field #1 (Extended Groth Strip), and Fields #3–4 are located in the SDSS deep survey strip (Stripe 82) for $u'g'r'i'z'$ imaging. Unfortunately, our galaxies in Field #2 lack SDSS data, thus they only have BRI imaging data. These

photometric data that we use have been compiled by Matthews et al. (2013).

We cross-matched our sample against the catalog of Bundy et al. (2006), which contains JK photometry. Unfortunately, only two galaxies have a match with 2″ (radius). This is not a surprise since many of our galaxies have low stellar masses, as we demonstrate below. While photometric data redward of 5500Å are unavailable, the $BRI+ugriz$ data do cover the Balmer/4000Å break, which is sufficient for the purpose of having reasonable measurements of stellar mass. Future efforts will include acquiring infrared data to provide more robust stellar mass estimates.

To model the SED, we use the Fitting and Assessment of Synthetic Templates code (Kriek et al. 2009) with Bruzual & Charlot (2003) models and adopt a Chabrier (2003) IMF, exponentially-declining star formation histories (SFHs; i.e., τ models), one-fifth solar metallicity, and Cal00 reddening. We also correct the broad-band photometry for the contribution of nebular emission lines following the approach described in Ly14. This correction reduces the stellar mass estimates by 0.2 dex (average). The stellar masses are provided in Table 1 and are illustrated in Figure 4. The average (median) stellar masses are 4.9×10^8 $M_\odot$ (5.0×10^8) and span 7.1×10^7–2.2×10^9 $M_\odot$.

4. RESULTS

Figure 4 illustrates the dependence of our derived properties following different projections. Panel (a) illustrates the [O III]$\lambda5007$/Hβ flux ratios and stellar masses along the "Mass–Excitation" (MEx; Juneau et al. 2014) diagram. The MEx is used as a substitute for the Baldwin et al. (1981) diagnostic diagram when [N II]$\lambda6583$/Hα is unavailable. It can be seen that these galaxies have high [O III]/Hβ ratios, 5.0 ± 0.9. All of them are classified as star-forming galaxies by falling below the solid black line. Compared to other metal-poor galaxies (Ly14, blue squares), these galaxies have similar excitation properties, but are ≈0.4 dex more massive. Compared to UV- and mass-selected $z \sim 2$ galaxies (e.g., Shapley et al. 2014; Steidel et al. 2014), our measured [O III]/Hβ ratios are higher by a factor of 1.25–2.5. Their strong-line oxygen ratios, R_{23} and O_{32}, are consistent with $z \sim 2$ galaxies from Shapley et al. (2014).

Panel (b) compares the dust-corrected instantaneous SFRs against the stellar mass estimates. Here we compare our work against mass-selected galaxies at $z \sim 1$ (Whitaker et al. 2014b) and Hα-selected galaxies at $z \approx 0.8$ (de los Reyes et al. 2014). Our galaxies are located 1.05 ± 0.61 dex above these $M_\star$–SFR relations with SFR/$M_\star$ of $10^{-8.0\pm0.6}$ yr^{-1}. This significant SFR offset is also seen for metal-poor galaxies from Ly14. By requiring [O III]$\lambda4363$ detections, both [O III]$\lambda4363$ studies are biased toward high-EW emission lines (see Figure 2), which correspond to a higher sSFRs.

Panel (c) illustrates the $M_\star$–Z relation. Here we compare our results against AM13. In this study, they stacked $0.027 < z < 0.25$ SDSS spectra in bins of SFR and $M_\star$ to detect [O III]$\lambda4363$. Figure 4c illustrates that while a subset of our galaxies is consistent with AM13, a significant fraction (60%) are located below the relation at more than 0.22 dex (1σ; AM13), by as much as –0.76 dex. This results in an average Z offset for the sample of
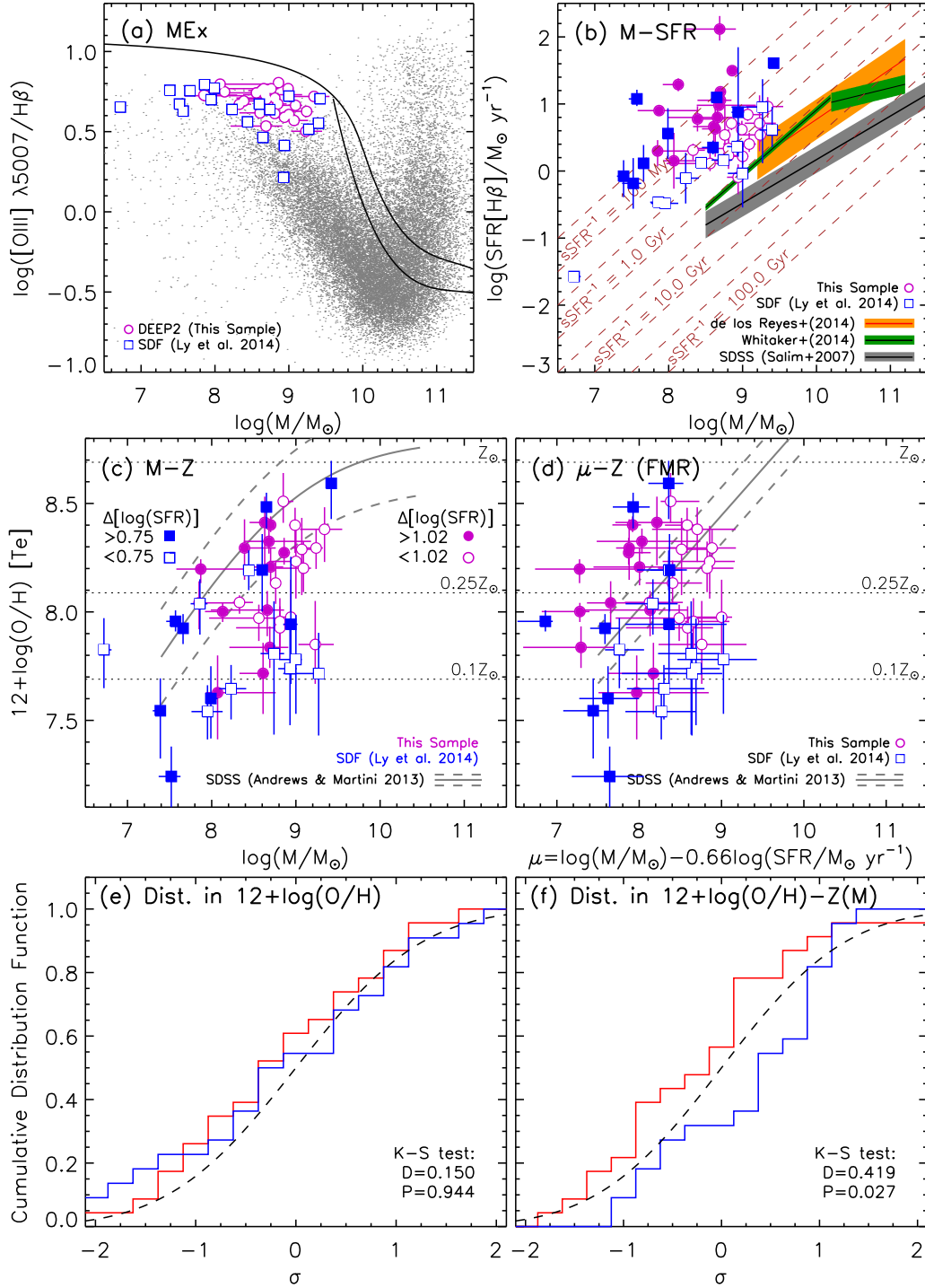
FIG. 4.— Relations between stellar mass and (a) "excitation" ([O III]/Hβ), (b) dust-corrected Hβ SFR, (c) metallicity, and (d) metallicity and dust-corrected Hβ SFR. The DEEP2 [O III]λ4363 sample is shown by the purple circles. Overlaid as blue squares is the Ly14 [O III]λ4363 sample. Results from the SDSS sample (Salim et al. 2007; Juneau et al. 2014; AM13) is illustrated in gray. For comparison, we also overlay in panel (b) the stellar mass–SFR relation of Hα-selected galaxies at $z = 0.8$ (de los Reyes et al. 2014) and mass-selected star-forming galaxies at $z = 0.5$–1 (Whitaker et al. 2014a) in orange and green, respectively. For direct metallicity comparisons, we illustrate the results of AM13, which stacked spectra to measure average T_e-based metallicities. Panels (e) and (f) show the cumulative distribution functions for two samples with low (open symbols in (b)–(d); blue line) and high SFRs (filled symbols; red line) when the DEEP2 and SDF samples are combined. The K-S statistics (D) and the probability that the two distributions are identical (P) are given in the lower right-hand corner.

-0.28 ± 0.23 dex. Our $M_\star$–Z relation result is consistent with Ly14 (blue squares), who also found that half of their sample falls below the local $M_\star$–Z relation.

The FMR was introduced to describe the dependence between $M_\star$, Z, and SFR in local galaxies, and was extended to explain higher redshift galaxies. Mannucci et al. (2010) was one of the first studies to parameterize this dependence by considering a combination of stellar mass and SFR:

$$\mu = \log(M_\star) - \alpha \log(\text{SFR}), \quad (3)$$

where α is the coefficient that minimizes the scatter against metallicity. Figure 4d illustrates the μ projection of the $M_\star$–Z–SFR relation with $\alpha = 0.66$ (AM13). It can be seen that our sample is consistent $(0.01 \pm 0.29$ dex) with the local FMR; however significant dispersion remains. The dispersion is greater than our $M_\star$–Z comparison and the average measurement uncertainties of ≈ 0.16 dex.

The local $M_\star$–Z–SFR relation suggests that higher SFR galaxies have lower metallicity at fixed stellar mass. To examine if this is correct, we split our sample and the SDF (Ly14) by high and low sSFRs, illustrated in Figure 4b–d as filled and opened symbols, respectively. The sample is divided at the median $\Delta[\log(\text{SFR})]$, which is the amount of deviation relative to the Whitaker et al. (2014a) $M_\star$–SFR relation. This relative SFR offset follows the non-parametric approach of Salim et al. (2014). We then perform Kolmogorov-Smirnoff (K-S) tests to determine if these two distributions are different. We compare the $\log(\text{O/H})$ distributions for the low- and high-SFR samples, finding that these two distributions are similar (see Figure 4e). However, as Figure 4b shows, these two samples differ in stellar mass by ≈ 0.4 dex. If instead we consider the relative offset in metallicity against the $M_\star$–Z relation of AM13, the K-S test finds that the two samples are different at 97.3% $(2.1\sigma$; Figure 4f). The difference, however, is in the opposite direction of local predictions, with higher sSFR galaxies having higher gas-phase metallicities. This is evident in Figure 4c at $M_\star \approx 10^{8.6}$ $M_\odot$ (where the two samples overlap) as the low-SFR galaxies have $12 + \log(\text{O/H}) \leq 8.2$ while the high-SFR sample spans $12 + \log(\text{O/H}) =$ 7.7–8.5.

5. DISCUSSIONS

From DEEP2 spectra of 28 galaxies with oxygen abundances from [O III]λ4363 detections (i.e., the T_e method), we find that metal-poor strongly star-forming galaxies are consistent with the local FMR (AM13), albeit with large dispersion (0.29 dex with 0.16 dex due to measurement errors). This result is consistent with metal-poor galaxies from Ly et al. (2014), and lensed low-mass star-forming galaxies at $z \sim 0.8$–2.6 (Wuyts et al. 2012). Given the high sSFRs of $\sim(100 \text{ Myr})^{-1}$, we argue that the large dispersion in metallicity is unsurprising—these galaxies are most likely undergoing episodic star formation and have not settled into a steady state.

We find marginal (97.3%; 2.1σ) evidence that galaxies with higher sSFRs $(\lesssim 10^{-8}$ yr$^{-1})$ are more metal-rich. While this contradicts previous local studies, the inverse of the sSFR—timescale for star formation—is short. Assuming outflow velocities comparable to virial velocities $(\sim 150$ km s$^{-1})$ for $\log(M_{\text{halo}}/M_\odot) \approx 11.1$ (Behroozi et al. 2010), 8 galaxies in our sample would not have enough time (sSFR$^{-1} \lesssim 10^{7.65}$ yr) for any recently enriched outflows to be driven out of the $1''$ (7.5 kpc) slit-widths. Thus, one would expect the SFR–Z dependence to turn positive for low-mass strongly star-forming galaxies. Given the instantaneous SFRs, we find that the measured oxygen abundances can be explained with low nucleosynthesis yields $(y \sim 0.01)$, gas-to-stellar mass fraction of $\approx 1 \pm 0.4$, and no metal loss due to outflows.

REFERENCES

Aller, L. H. 1984, Astrophysics and Space Science Library, (Dordrecht: Reidel)

Andrews, B. H., & Martini, P. 2013, ApJ, 765, 140 [AM13]

Baldwin, A., Phillips, M. M., & Terlevich, R. 1981, PASP, 93, 817

Berg, D. A., Skillman, E. D., Marble, A. R., et al. 2012, ApJ, 754, 98

Behroozi, P. S., Conroy, C., & Wechsler, R. H. 2010, ApJ, 717, 379

Brown, W. R., Kewley, L. J., & Geller, M. J. 2008, AJ, 135, 92

Bruzual, G., & Charlot, S. 2003, MNRAS, 344, 1000

Bundy, K., Ellis, R. S., Conselice, C. J., et al. 2006, ApJ, 651, 120

Calzetti, D., Armus, L., Bohlin, R. C., Kinney, A. L., Koornneef, J., & Storchi-Bergmann, T. 2000, ApJ, 533, 682 [Cal00]

Chabrier, G. 2003, PASP, 115, 763

Coil, A. L., Newman, J. A., Kaiser, N., et al. 2004, ApJ, 617, 765

Davé, R., Finlator, K., & Oppenheimer, B. D. 2011, MNRAS, 416, 1354

Davis, M., Faber, S. M., Newman, J., et al. 2003, Proc. SPIE, 4834, 161

de los Reyes, M., Ly, C., Lee, J. C., 2014, AJ, in press (arXiv:1410.1551)

Ellison, S. L., Patton, D. R., Simard, L., & McConnachie, A. W. 2008, ApJ, 672, L107

Faber, S. M., Phillips, A. C., Kibrick, R. I., et al. 2003, Proc. SPIE, 4841, 1657

Henry, A., Martin, C. L., Finlator, K., & Dressler, A. 2013a, ApJ, 769, 148

Henry, A., Scarlata, C., Domínguez, A., et al. 2013b, ApJ, 776, L27

Hunt, L., Magrini, L., Galli, D., et al. 2012, MNRAS, 427, 906

Hoyos, C., Koo, D. C., Phillips, A. C., Willmer, C. N. A., & Guhathakurta, P. 2005, ApJ, 635, L21

Hu, E. M., Cowie, L. L., Kakazu, Y., & Barger, A. J. 2009, ApJ, 698, 2014

Izotov, Y. I., Stasińska, G., Meynet, G., Guseva, N. G., & Thuan, T. X. 2006, A&A, 448, 955

Izotov, Y. I., Thuan, T. X., & Guseva, N. G. 2012, A&A, 546, A122

Juneau, S., Bournaud, F., Charlot, S., et al. 2014, ApJ, 788, 88

Kennicutt, R. C. 1998, ARA&A, 36, 189

Kriek, M., van Dokkum, P. G., Labbé, I., Franx, M., Illingworth, G. D., Marchesini, D., & Quadri, R. F. 2009, ApJ, 700, 221

Lara-López, M. A., Cepa, J., Bongiovanni, A., et al. 2010, A&A, 521, L53

Liu, X., Shapley, A. E., Coil, A. L., Brinchmann, J., & Ma, C.-P. 2008, ApJ, 678, 758

Ly, C., Malkan, M. A., Hayashi, M., et al. 2011, ApJ, 735, 91

Ly, C., Malkan, M. A., Kashikawa, N., et al. 2012, ApJ, 757, 63

Ly, C., Malkan, M. A., Nagao, T., et al. 2014, ApJ, 780, 122 [Ly14]

Mannucci, F., Cresci, G., Maiolino, R., Marconi, A., & Gnerucci, A. 2010, MNRAS, 408, 2115

Markwardt, C. B. 2009, Astronomical Data Analysis Software and Systems XVIII, 411, 251

Matthews, D. J., Newman, J. A., Coil, A. L., Cooper, M. C., & Gwyn, S. D. J. 2013, ApJS, 204, 21

McGaugh, S. S. 1991, ApJ, 380, 140

Moustakas, J., Zaritsky, D., Brown, M., et al. 2011, ApJ, submitted (arXiv:1112.3300)

Newman, J. A., Cooper, M. C., Davis, M., et al. 2013, ApJS, 208, 5

Nicholls, D. C., Dopita, M. A., Sutherland, R. S., Kewley, L. J., & Palay, E. 2013, ApJS, 207, 21

Pagel, B. E. J., Edmunds, M. G., Blackwell, D. E., Chun, M. S., & Smith, G. 1979, MNRAS, 189, 95

Peeples, M. S., & Shankar, F. 2011, MNRAS, 417, 2962

Rigby, J. R., Wuyts, E., Gladders, M. D., Sharon, K., & Becker, G. D. 2011, ApJ, 732, 59

Salim, S., Rich, R. M., Charlot, S., et al. 2007, ApJS, 173, 267

Salim, S., Lee, J. C., Ly, C., et al. 2014, ApJ, in press (arXiv:1411.7391)

Shapley, A. E., Reddy, N. A., Kriek, M., et al. 2014, ApJ, submitted (arXiv:1409.7071)

Steidel, C. C., Rudie, G. C., Strom, A. L., et al. 2014, ApJ, in press (arXiv:1405.5473)

Tremonti, C. A., Heckman, T. M., Kauffmann, G., et al. 2004, ApJ, 613, 898

Whitaker, K. E., Franx, M., Leja, J., et al. 2014a, ApJ, 795, 104

Whitaker, K. E., Rigby, J. R., Brammer, G. B., et al. 2014b, ApJ, 790, 143

Wuyts, E., Rigby, J. R., Sharon, K., & Gladders, M. D. 2012, ApJ, 755, 73

Xia, L., Malhotra, S., Rhoads, J., et al. 2012, AJ, 144, 28

TABLE 1
SUMMARY OF DEEP2 SAMPLE

ID	R.A. (hh:mm:ss)	Declination (dd:mm:ss)	z	EW(Hβ) (Å)	$\log(M_\star/M_\odot)$	$\log\left[\frac{SFR_{H\beta}}{M_\odot\ yr^{-1}}\right]$	$E(B{-}V)$ (mag)	S/N ($\lambda4363$)	[O II]/Hβ	[O III]/Hβ	$\frac{[O\,III]}{[O\,III]\lambda4363}$	$\log(T_e/K)$	$12+\log(O/H)$
01	14:18:31.260	52:49:42.545	0.8194	38.46	$8.81^{+0.18}_{-0.00}$	0.23 ± 0.16	$0.00^{+0.09}_{-0.08}$	4.9	$2.165^{+0.101}_{-0.051}$	$5.507^{+0.156}_{-0.067}$	$57.273^{+11.748}_{-08.811}$	4.18 ± 0.04	$7.96^{+0.11}_{-0.14}$
02	14:21:21.513	53:01:07.672	0.7496	51.94	$8.76^{+0.04}_{-0.06}$	$0.54^{+0.45}_{-0.33}$	$0.28^{+0.24}_{-0.18}$	5.9	$1.821^{+0.705}_{-0.235}$	$7.792^{+0.200}_{-0.351}$	$67.843^{+19.856}_{-06.619}$	4.14 ± 0.04	8.13 ± 0.10
03	14:21:25.487	53:09:48.071	0.7099	104.49	$8.94^{+0.00}_{-0.15}$	$-0.09_{-0.25}$	$0.00^{+0.10}_{-0.14}$	3.7	2.413 ± 0.103	$5.178^{+0.198}_{-0.085}$	$54.985^{+20.947}_{-10.473}$	$4.17^{+0.06}_{-0.05}$	$7.98^{+0.17}_{-0.19}$
04	14:22:03.718	53:25:47.766	0.7878	7.38	…	$-0.06^{+0.63}_{-0.59}$	$0.00^{+0.34}_{-0.32}$	5.5	0.867 ± 0.094	$7.273^{+0.385}_{-0.578}$	$18.192^{+05.923}_{-01.692}$	$4.49^{+0.08}_{-0.07}$	$7.35^{+0.11}_{-0.17}$
05	14:21:45.408	53:23:52.699	0.7710	74.51	$8.86^{+0.07}_{-0.00}$	$1.50^{+0.07}_{-0.05}$	$0.47^{+0.04}_{-0.03}$	10.0	1.960 ± 0.084	$8.497^{+0.080}_{-0.133}$	$90.482^{+10.167}_{-08.133}$	4.10 ± 0.02	$8.27^{+0.07}_{-0.06}$
06	16:47:26.188	34:45:12.126	0.7166	36.91	$8.85^{+0.12}_{-0.01}$	$0.71^{+0.07}_{-0.10}$	$0.21^{+0.04}_{-0.05}$	5.0	$2.539^{+0.221}_{-0.095}$	6.245 ± 0.081	$131.237^{+47.723}_{-15.908}$	$4.02^{+0.02}_{-0.03}$	$8.51^{+0.13}_{-0.10}$
07	16:46:35.420	34:50:27.928	0.7624	34.71	$9.07^{+0.19}_{-0.00}$	$0.84^{+0.12}_{-0.10}$	$0.22^{+0.07}_{-0.05}$	3.4	$3.304^{+0.208}_{-0.260}$	$5.003^{+0.040}_{-0.081}$	$83.493^{+25.690}_{-12.845}$	4.09 ± 0.05	$8.29^{+0.15}_{-0.21}$
08	16:47:26.488	34:54:09.770	0.7653	79.33	$8.07^{+0.69}_{-0.14}$	0.15 ± 0.42	0.22 ± 0.23	4.0	$1.412^{+0.779}_{-0.097}$	$7.866^{+0.589}_{-0.168}$	$24.249^{+08.434}_{-04.217}$	$4.38^{+0.08}_{-0.11}$	$7.63^{+0.17}_{-0.21}$
09	16:49:51.368	34:45:18.210	0.7909	53.06	$9.00^{+0.08}_{-0.32}$	$0.22^{+0.17}_{-0.12}$	$0.02^{+0.09}_{-0.07}$	3.6	$2.496^{+0.197}_{-0.079}$	$5.485^{+0.124}_{-0.099}$	$78.655^{+29.964}_{-14.982}$	$4.10^{+0.05}_{-0.04}$	$8.23^{+0.16}_{-0.17}$
10	16:51:31.472	34:53:15.964	0.7945	64.52	$8.70^{+0.15}_{-0.31}$	1.06 ± 0.08	0.31 ± 0.04	6.4	$2.159^{+0.093}_{-0.140}$	$6.739^{+0.094}_{-0.040}$	$85.109^{+15.474}_{-12.379}$	$4.11^{+0.02}_{-0.03}$	$8.21^{+0.09}_{-0.08}$
11	16:50:55.342	34:53:29.875	0.7980	94.85	$8.56^{+0.21}_{-0.59}$	$0.11^{+0.16}_{-0.11}$	$0.00^{+0.08}_{-0.06}$	7.7	2.086 ± 0.065	$7.480^{+0.148}_{-0.118}$	$58.301^{+03.195}_{-11.181}$	4.19 ± 0.03	$7.97^{+0.06}_{-0.11}$
12	16:53:03.486	34:58:48.946	0.7488	69.05	$8.33^{+0.16}_{-0.08}$	$0.31^{+0.10}_{-0.15}$	$0.06^{+0.05}_{-0.08}$	13.2	$1.702^{+0.229}_{-0.000}$	$6.384^{+0.130}_{-0.056}$	$70.872^{+04.765}_{-05.956}$	$4.15^{+0.02}_{-0.01}$	$8.04^{+0.03}_{-0.05}$
13	16:51:24.060	35:01:38.740	0.7936	32.65	$9.09^{+0.09}_{-0.35}$	$0.40^{+0.17}_{-0.12}$	$0.23^{+0.09}_{-0.06}$	5.2	$2.862^{+0.369}_{-0.185}$	$6.241^{+0.154}_{-0.103}$	$74.343^{+15.250}_{-11.437}$	$4.13^{+0.03}_{-0.04}$	$8.20^{+0.12}_{-0.11}$
14	16:51:20.343	35:02:32.628	0.7936	135.97	$8.68^{+0.50}_{-0.30}$	$0.98^{+0.08}_{-0.06}$	0.21 ± 0.04	9.3	2.173 ± 0.089	$7.209^{+0.040}$	$105.147^{+12.086}_{-09.669}$	$4.07^{+0.01}_{-0.02}$	8.33 ± 0.06
15	23:27:20.369	00:05:54.762	0.7553	741.71	$8.13^{+0.01}_{-0.21}$	$1.29^{+0.09}_{-0.10}$	0.48 ± 0.05	13.6	$1.034^{+0.096}_{-0.027}$	$7.428^{+0.084}_{-0.042}$	$72.096^{+04.614}_{-06.921}$	$4.15^{+0.01}_{-0.02}$	$8.00^{+0.04}_{-0.05}$
16	23:27:43.140	00:12:42.832	0.7743	34.15	$9.23^{+0.22}_{-0.20}$	0.71 ± 0.42	0.22 ± 0.23	3.4	$1.958^{+0.945}_{-0.000}$	4.320 ± 0.124	$46.844^{+18.738}_{-12.492}$	4.21 ± 0.07	$7.85^{+0.20}_{-0.18}$
17	23:27:29.854	00:14:20.439	0.7637	40.62	$8.39^{+0.37}_{-0.01}$	0.78 ± 0.19	0.32 ± 0.10	4.3	$2.420^{+0.596}_{-0.074}$	$6.508^{+0.147}_{-0.074}$	$89.583^{+28.898}_{-17.339}$	4.09 ± 0.04	$8.29^{+0.13}_{-0.15}$
18	23:27:07.500	00:17:41.503	0.7885	49.03	$9.34^{+0.21}_{-0.29}$	$0.96^{+0.14}_{-0.17}$	$0.34^{+0.08}_{-0.09}$	4.4	$1.794^{+0.129}_{-0.194}$	7.022 ± 0.113	$115.500^{+37.258}_{-14.903}$	4.04 ± 0.04	$8.38^{+0.10}_{-0.15}$
19	23:26:55.430	00:17:52.919	0.8562	97.37	$8.99^{+0.00}_{-0.07}$	$0.62^{+0.13}_{-0.08}$	$0.00^{+0.07}_{-0.04}$	5.2	$1.636^{+0.021}_{-0.026}$	$7.989^{+0.066}_{-0.132}$	$128.952^{+17.993}_{-23.991}$	$4.04^{+0.03}_{-0.02}$	$8.40^{+0.08}_{-0.13}$
20	23:30:57.949	00:03:38.191	0.7842	87.95	$8.61^{+0.07}_{-0.28}$	$0.66^{+0.18}_{-0.26}$	$0.26^{+0.10}_{-0.14}$	4.1	$2.017^{+0.276}_{-0.221}$	$5.575^{+0.132}_{-0.159}$	$36.499^{+14.600}_{-05.840}$	$4.26^{+0.05}_{-0.09}$	$7.72^{+0.14}_{-0.19}$
21	23:31:50.728	00:09:39.393	0.8225	63.83	$8.81^{+0.06}_{-0.52}$	$0.34^{+0.29}_{-0.30}$	$0.09^{+0.16}_{-0.17}$	5.0	$1.692^{+0.344}_{-0.115}$	$6.989^{+0.179}_{-0.223}$	$52.462^{+11.343}_{-08.507}$	$4.19^{+0.05}_{-0.04}$	$7.93^{+0.10}_{-0.14}$
22	02:27:48.871	00:24:40.077	0.7838	298.74	$7.85^{+0.45}_{-0.06}$	$0.30^{+0.16}_{-0.23}$	$0.07^{+0.09}_{-0.13}$	5.3	$1.735^{+0.343}_{-0.043}$	$7.110^{+0.103}_{-0.207}$	$61.688^{+12.654}_{-09.490}$	$4.16^{+0.03}_{-0.04}$	$8.04^{+0.10}_{-0.12}$
23	02:27:05.706	00:25:21.865	0.7661	77.52	$8.63^{+0.07}_{-0.18}$	0.63 ± 0.42	0.22 ± 0.23	3.2	$1.492^{+0.720}_{-0.000}$	$7.631^{+0.135}_{-0.108}$	$144.017^{+00.000}_{-57.607}$	$4.05^{+0.05}_{-0.06}$	$8.41^{+0.12}_{-0.20}$
24	02:27:30.457	00:31:06.391	0.7214	159.58	$7.87^{+0.52}_{-0.29}$	$0.90^{+0.07}_{-0.06}$	0.25 ± 0.04	9.6	1.525 ± 0.076	7.105 ± 0.057	$94.916^{+08.344}_{-10.430}$	4.09 ± 0.02	$8.20^{+0.05}_{-0.06}$
25	02:26:03.707	00:36:22.460	0.7888	66.11	$8.69^{+0.22}_{-0.48}$	$2.12^{+0.20}_{-0.17}$	$1.02^{+0.11}_{-0.09}$	6.6	$2.857^{+0.269}_{-0.336}$	$4.878^{+0.130}_{-0.065}$	$48.598^{+05.116}_{-08.526}$	$4.23^{+0.04}_{-0.03}$	$7.84^{+0.10}_{-0.09}$
26	02:26:21.479	00:48:06.813	0.7743	36.94	$9.24^{+0.08}_{-0.29}$	$0.54^{+0.10}$	$0.00^{+0.05}_{-0.06}$	6.7	$2.064^{+0.031}_{-0.041}$	$5.895^{+0.089}_{-0.044}$	109.091 ± 14.307	4.07 ± 0.02	$8.29^{+0.08}_{-0.10}$
27	02:29:33.654	00:26:08.023	0.7294	67.55	$8.66^{+0.20}_{-0.67}$	$0.80^{+0.14}_{-0.20}$	$0.36^{+0.08}_{-0.11}$	7.0	$2.555^{+0.220}_{-0.330}$	$7.849^{+0.132}_{-0.231}$	$54.969^{+09.644}_{-07.715}$	4.19 ± 0.04	$8.01^{+0.09}_{-0.12}$
28	02:29:02.031	00:30:08.127	0.7315	99.97	$8.70^{+0.01}_{-0.06}$	$1.18^{+0.03}_{-0.04}$	0.30 ± 0.02	15.2	$1.515^{+0.042}_{-0.028}$	$7.633^{+0.037}_{-0.019}$	$132.444^{+10.667}_{-05.333}$	4.04 ± 0.01	$8.40^{+0.04}_{-0.03}$

NOTE. — Unless otherwise specified, [O III] refers to [O III]$\lambda\lambda$4959,5007.